Computer Methods in Biomechanics and Biomedical Engineering, 2002 Vol. 5 (4), pp. 319–328

Flow-induced Wall Shear Stress in Abdominal Aortic Aneurysms: Part II – Pulsatile Flow Hemodynamics

ENDER A. FINOL* and CRISTINA H. AMON

Mechanical Engineering, Biomedical and Health Engineering, and Institute for Complex Engineered Systems, Carnegie Mellon University, Pittsburgh, PA

(Received 18 September 2000; In final form 6 March 2001)

In continuing the investigation of AAA hemodynamics, unsteady flow-induced stresses are presented for pulsatile blood flow through the double-aneurysm model described in Part I. Physiologically realistic aortic blood flow is simulated under pulsatile conditions for the range of time-average Reynolds numbers $50 \leq \mathrm{Re_m} \leq 300$. Hemodynamic disturbance is evaluated for a modified set of indicator functions which include wall pressure (p_w), wall shear stress (τ_w), Wall Shear Stress Gradient (WSSG), time-average wall shear stress ($\overline{\tau_w}$*), and time–average Wall Shear Stress Gradient $\overline{\mathrm{WSSG}}$*. At peak flow, the highest shear stress and WSSG levels are obtained at the distal end of both aneurysms, in a pattern similar to that of steady flow. The maximum values of wall shear stresses and wall shear stress gradients are evaluated as a function of the time–average Reynolds number resulting in a fourth order polynomial correlation. A comparison between numerical predictions for steady and pulsatile flow is presented, illustrating the importance of considering time-dependent flow for the evaluation of hemodynamic indicators.

Keywords: Hemodynamics; Aneuryms; Pulsatile flow; Shear stress; Wall shear stress gradient

INTRODUCTION

Several experimental and numerical investigations of pulsatile flow in AAAs are found in the literature. The first numerical study of pulsatile blood flow in aneurysms, conducted by Wille [1], demonstrated the presence of a recirculation region of variable size and intensity throughout the cardiac cycle. Representation of pulsatile flow patterns has been performed using velocity vectors and particle paths through axisymmetric aneurysm models [2]. The first combined experimental and numerical study of pulsatile flow in AAAs [3] showed the existence of primary and secondary vortices, and relatively high pressure fluctuations at the distal end of an aneurysm model. Three-dimensional unsteady flow simulations [4] resulted in the prediction of the appearance and disappearance of the primary vortex, and regions of high wall shear stresses both at the proximal and distal edge. Elger *et al.* [5], performed numerical simulations of pulsatile flow in an axisymmetric single-aneurysm model, illustrating streamline patterns and their effect on wall shear stresses and pressure distributions. Parametric studies demonstrated the little influence the bulge model and the vortex dynamics have on wall pressure distributions. The flow frequency, however, has the most significant effect on the magnitudes of wall pressure and wall shear stresses [6]. Correlation between steady flow dynamics and rates of platelet deposition proved the existence of a monotonic increase of platelet aggregation at the aneurysm wall, until reaching a maximum downstream of the aneurysm model [7]. Guzmán and Amon [8], and Amon *et al.* [9], have studied the temporal flow evolution of laminar, transitional and chaotic flow in converging–diverging channels using a geometry similar to that investigated in this work. Boundary layer separation during pulsatile flow has been seen ahead and behind the recirculation regions within an aneurysm model [10]. Direct numerical simulations of non-Newtonian flow through double-aneurysm models have been conducted under pulsatile conditions, resulting in flow patterns and wall shear stresses that were underestimated for otherwise Newtonian flow behavior [11]. Guzmán *et al.* [12],

*Corresponding author. Tel.: (412) 268-2497/2491/2511/3689. Fax: (412) 268-3348. E-mail: finol@andrew.cmu.edu

ISSN 1025-5842 print/ISSN 1476-8259 online © 2002 Taylor & Francis Ltd
DOI: 10.1080/1025584021000009751

performed validation studies of pulsatile non-Newtonian flow simulations by means of three asymptotic cases that take into account geometric inhomogeneities in the model. Resting and exercise conditions have been investigated both experimentally and numerically in AAA models [13]. Studies conducted by Peattie and Bluth [14] suggest that aneurysm diameter has little effect on the wall pressure distribution and its magnitude over the flow cycle. Particle Image Velocimetry (PIV) has been used to characterize steady and time-dependent flow (by means of a sinusoidal waveform) in aneurysm models over a wide range of physiological parameters [15].

In addition to the evaluation of hemodynamic forces due to inlet flow characteristics and irregular geometries on the rigid arterial models described above, endothelial cell culture studies have also been performed in order to quantify the response of the arterial wall. Recent investigations demonstrate the existence of diverse cell responses under low levels of shear stress, but large *shear stress gradients*. Disturbed flow patterns at different magnitudes of shear stress gradients have been found to trigger responses of the innermost layer of the tunica intima by altering intercellular communication mechanisms [16,17]. Grabowski [18] suggests that the artery wall is subject to three flow-induced forces that result from (a) fluid shear stress, (b) transmural pressure, and (c) wall stretching and flexion.

To evaluate the interaction of high and low shear stresses in a region where intraluminal thrombus is most likely to be promoted, we propose the quantification of hemodynamic disturbance in pulsatile flow through AAAs, by means of distributions of Wall Shear Stress Gradients (WSSGs). Time–average nondimensional wall shear stress ($\overline{\tau_w}^*$) and time–average nondimensional Wall Shear Stress Gradient $\overline{\mathrm{WSSG}}^*$ distributions are presented as a function of different flow conditions. Additionally, a correlation is developed for the maximum values of wall shear stress and WSSG as a function of the time–average Reynolds number.

MATHEMATICAL FORMULATION

The governing equations and artery geometry are described in Part I of this investigation [19]. For pulsatile flow conditions, the inflow mean velocity is time-dependent and the volume flow rate has an oscillatory nature, as shown in Figure 1. Representation of the pulsatile waveform is done by a discrete Fourier series [20] based on the *in-vivo* measurement reported first by Mills *et al.* [21]. Figure 1 shows a triphasic pulse appropriate for average resting conditions, which are generally represented by $\mathrm{Re_m} \approx 300$ and $\alpha \approx 12$, as indicated by Pedersen *et al.* [22] in the abdominal segment of the human aorta. The time dependency of the inflow mean velocity is imposed by the following Fourier representation:

$$\bar{u}(t) = A_o + \sum_{k=1}^{N} (A_k \cdot \cos 2\pi kt + B_k \cdot \sin 2\pi kt) \quad (1)$$

where $N = 18$ is the number of harmonics used. The natural frequency of the pulsatile flow is set to $\omega = 2\pi$ rad/s, with a period $T_P = 1$ s. The Womersley number, which characterizes the flow frequency, the geometry of the model and the fluid viscous properties is $\alpha = 11.5$. The amplitude coefficient of the pulsatile flow is $\gamma = 5.25$ and the peak systolic flow occurs at $t = 0.31$ s. The time–average Reynolds number is calculated as $\mathrm{Re_m} = D\bar{u}_m/\nu$, where $\bar{u}_m$ is the time–average inflow mean velocity.

Two indicator functions are used to quantify the effect of time-dependent flow patterns on the hemodynamics of AAAs. The first indicator is the time–average nondimensional Wall Shear Stress Gradient ($\overline{\mathrm{WSSG}}^*$):

$$\overline{\mathrm{WSSG}}^* = \frac{D}{2\tau_{wo}} \frac{1}{T_P} \int_0^{T_P} \sqrt{\left(\frac{\partial \tau_w}{\partial \hat{t}}\right)^2 + \left(\frac{\partial \tau_w}{\partial \hat{n}}\right)^2}\, dt \quad (2)$$

where the superscript $*$ denotes an instantaneous nondimensional wall shear stress gradient, calculated as

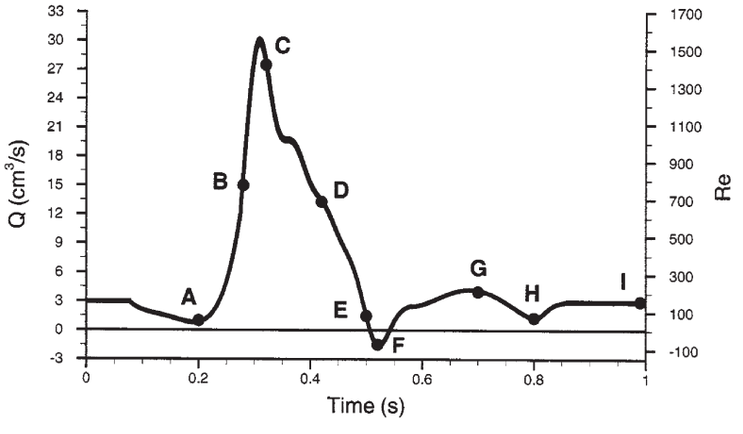

FIGURE 1 Pulsatile volumetric flow rate (Q) and instantaneous Reynolds number (Re) for $\mathrm{Re_m} = 300$. Flow stages A, B, …, I are of particular importance for the evaluation of hemodynamic indicators. Peak systolic flow occurs at $t = 0.31$ s and diastolic phase begins at $t = 0.52$ s.

$WSSG^* = ((WSSG)/(2\tau_{wo}/D))$, and τ_{wo} is the wall shear stress for fully developed flow in a healthy artery (Poiseuille flow), given by $\tau_{wo} = (8/\rho)(\mu/D)^2 Re_m$. The wall shear stress distribution is also calculated, and a time–average nondimensional wall shear stress serves as the second indicator:

$$\overline{\tau_w}^* = \frac{1}{\tau_{wo}} \frac{1}{T_P} \int_0^{T_P} \tau_w \, dt \tag{3}$$

where $\tau_w^* = \tau_w/\tau_{wo}$ is the instantaneous nondimensional wall shear stress.

RESULTS AND DISCUSSION

Numerical simulations for pulsatile flow are carried out at time–average Reynolds numbers over the range $50 < Re_m < 300$ ($262.5 < Re_{peak} < 1575$). Re_m is defined as the time–average Reynolds number obtained by integrating the instantaneous Reynolds number over the pulsatile cycle; the instantaneous Reynolds number, $Re_i(t_j)$ is based on the inflow mean velocity at time t_j. The pressure at the exit is set to 0 Pa and, thus, all the pressure results are relative to this value. Results are obtained at intervals of 1/50 second, but only the flow stages considered to be the ones that represent the most important hemodynamic changes during the cycle are presented in this section. These stages are obtained from the last cycle of the asymptotically converged temporal solution, which is reached after a transient resulting from the application of the initial condition. The initial condition applied is the converged velocity and pressure field at the last three time steps of the simulation corresponding to the immediately lower time–average Reynolds number. For example, the initial condition for the $Re_m = 200$ cycle is the converged velocity and pressure field at the last three time steps of the $Re_m = 150$ cycle. Regardless of the initial condition applied, the output of a numerical simulation is the same as long as it overcomes the initial transient until the flow becomes time periodic. Therefore, a sufficient number of cycles must be performed numerically to overcome the transient period until temporal convergence is achieved. This is verified by analyzing velocity and pressure history at different points of the computational domain, as shown in Figure 2 for $Re_m = 300$. The initial value code solves the fully discrete set of governing equations at each time step by means of iterative solvers and tensor-product sum-factorization techniques.

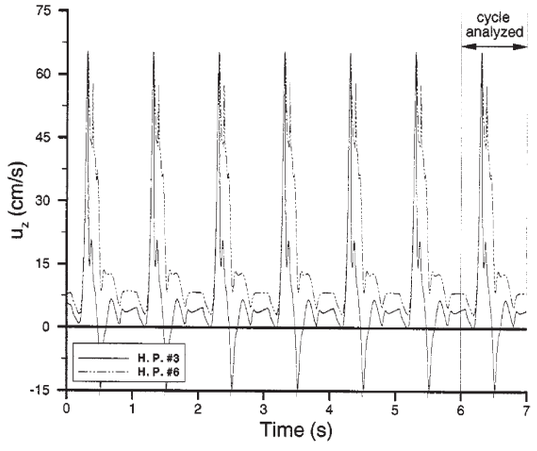

FIGURE 2 Temporal evolution of the axial velocity for $Re_m = 300$ at history points #3 and #6 (shown in Fig. 1–Part I [19]) of the computational domain.

Vortex Structure

Streamline plots for three representative Reynolds numbers are shown in Figure 3: $Re_m = 100$ ($Re_{Peak} = 525$), $Re_m = 200$ ($Re_{peak} = 1050$), and $Re_m = 300$ ($Re_{peak} = 1575$). They represent the vortex structures at eight flow stages (A–D and F–I) depicted on the pulsatile flow waveform in Figure 1. The residual vortices left from the last cycle are present within the two aneurysms at $t = 0.00$ s. The early systolic phase of the flow cycle is characterized by a constant flow rate until $t = 0.08$ s and an immediate deceleration until $t = 0.20$ s. The stronger, systolic ventricular pumping begins at $t = 0.20$ s until reaching peak flow at $t = 0.31$ s. The fluid is then subject to a reduction of its inflow mean velocity for $0.08\,s < t \leq 0.20\,s$ causing negative velocity gradients and an increase in size of the recirculation regions. A large pressure gradient follows, and the temporal acceleration of the blood is much larger for the interval $0.20\,s < t \leq 0.31\,s$ than the convective deceleration originated by the proximally diverging walls of the artery. The local deceleration experienced by the fluid entering the small aneurysm is weaker than in the large aneurysm and, thus, the favorable pressure gradient ejects the vortex in the small aneurysm first, for all three Reynolds numbers. Therefore, the steady-flow-like pattern [19] seen in frame A of Figure 3 is no longer maintained as the high velocity core flow ejects the low recirculating velocity regions downstream and the flow reattaches to the wall (frame B).

The flow begins to decelerate temporally during the period given by $0.31\,s < t < 0.50\,s$. A higher Reynolds number yields stronger temporal decelerations and a faster vortex formation. At $t = 0.32$ s, near peak flow, a recirculating region fills completely the small aneurysm for $Re_m = 300$. The vortex in the large aneurysm begins to grow for $Re_m = 200$ and increases in size for $Re_m = 300$. At $t = 0.42$ s and $Re_m = 200$, it has occupied the entire aneurysm inducing a clockwise rotating vortex against the proximal wall. For low-Reynolds number flows ($Re_m = 100$), the remainder of the systolic phase is characterized by vortex growth and its displacement downstream. For $Re_m = 300$, the vortices fill the aneurysms at an early stage of systolic deceleration, so that by the onset of diastole ($t = 0.52$ s) they have grown in size and intensity to induce vortex shedding of the secondary recirculation regions located against the wall of the large aneurysm.

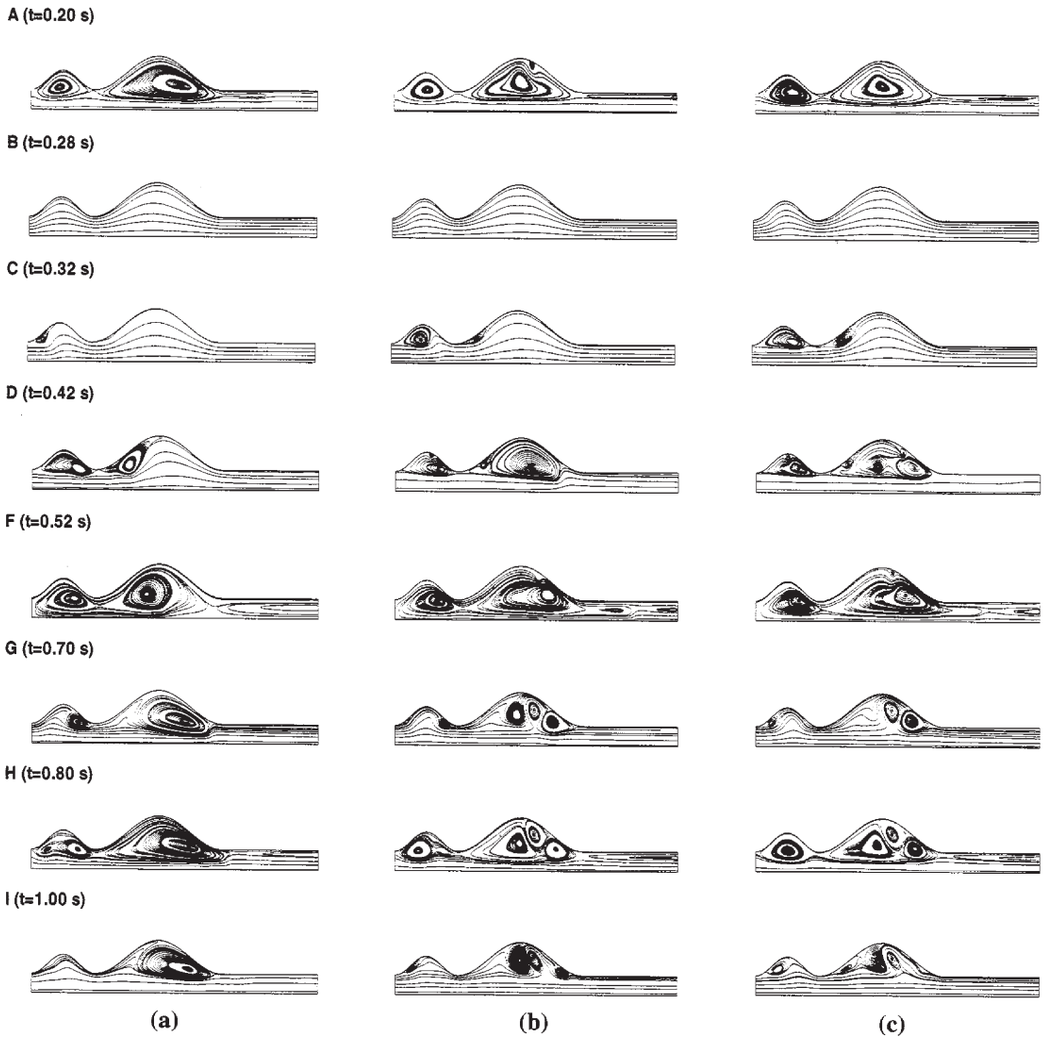

FIGURE 3 Streamlines for pulsatile flow at (a) $Re_m = 100$, (b) $Re_m = 200$, and (c) $Re_m = 300$. The direction of the flow is from left to right.

The interval $0.51\,s \leq t \leq 0.54\,s$ represents the negative flow period of the cycle. During this interval there is a reversal of the flow direction, which is shown by the right-to-left orientation of the streamlines within the end-tube at $t = 0.52\,s$. For $Re_m = 200$ and $Re_m = 300$, there is mixing of the retrograde flow with the recirculating flow inside the aneurysms, and the few undisturbed streamlines located near the centerline indicate the significant reduction of the core flow through the model. The addition of an end-tube to the double-aneurysm model is required to impose a zero-traction (outflow) condition farther downstream from the large aneurysm. Therefore, the imposed condition does not affect the flow dynamics within the model. Using a longer end-tube (of length greater than 3.75 inlet diameters) would only allow for a better development of the recirculation regions downstream of the large aneurysm at specific stages of the cycle (frames A, F, and H in Fig. 3), but would not influence the vortex structure inside the aneurysms.

The onset of diastole is at $t = 0.52\,s$ with a moderate temporal acceleration of the flow that ends at $t = 0.70\,s$. For $Re_m = 100$, this period results in a partial ejection of the small vortex and a reduction in size of the large one. For $Re_m = 200$ and $Re_m = 300$, the phase is characterized by an almost complete ejection of the small vortex, the coexistence of three vortices in the large aneurysm, and the presence of a core flow region at the center of the artery model in the left-to-right direction. Diastolic deceleration occurs for the period $0.70\,s < t \leq 0.80\,s$, producing an adverse pressure gradient that results in the entrapment of the three slow-rotating vortices within the large aneurysm. For $0.80\,s < t < 0.86\,s$, the moderate acceleration of the flow yields the ejection of the recirculation regions inside the end-tube, and a reduction in size of the small vortex and the three vortices in the large aneurysm. Late diastole is characterized by a constant flow rate that lasts until the next cycle ($0.86\,s \leq t \leq 1.08\,s$). During this period the vortex dynamics does not change, a core flow region is present near the

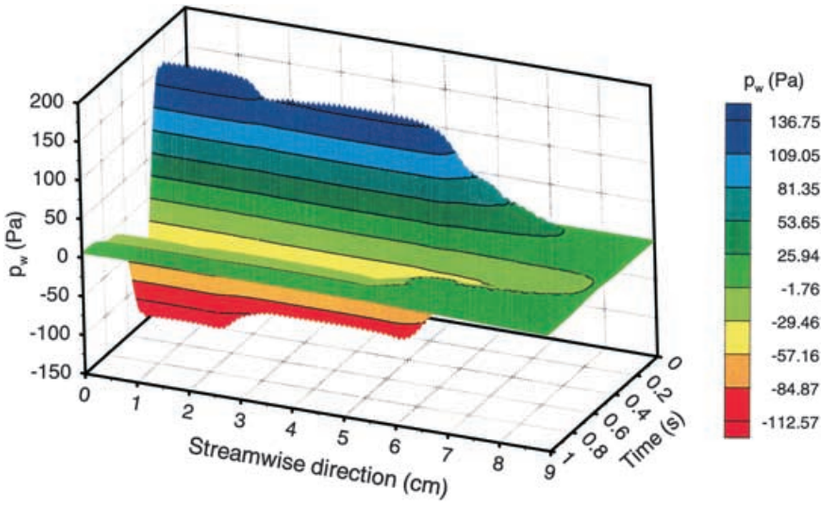

FIGURE 4 Wall pressure distribution for $Re_m = 300$ as a function of time and axial location.

centerline with a straightening of the streamlines at the exit, and the vortices present within the aneurysms remain nearly stagnant due to the absence of flow acceleration.

Wall Pressure

The time-dependent pressure distribution along the artery wall for $Re_m = 300$ is shown in Figure 4. It is important to mention that this three-dimensional distribution represents only a trend of the actual temporal variation of the wall pressure, since it is obtained by applying a second-order graphical smoothing technique to the p_w indicator. Figures 5 and 6 are also obtained using this smoothing technique. Our intent with Figures 4–6 is to discuss qualitatively the dependence of the hemodynamic indicators (p_w, τ_w and WSSG) on the axial location and temporal distribution of the vortex structures, for $Re_m = 300$. Exact (quantitative) distributions of time–average indicators are depicted in Figures 7 and 8 and the maximum values of the indicators are shown in Figures 9 and 10.

The pressure distribution at the arterial wall is largely influenced by the temporal accelerations and decelerations of the flow that occur during the pulsatile flow cycle. The largest favorable wall pressure gradients are obtained at mid-systolic acceleration ($t = 0.28$ s), and the largest adverse wall pressure gradients are obtained during late systolic deceleration ($t = 0.50$ s), as shown in Figure 4. However, at any given time of the cycle, the wall pressure remains nearly uniform along most of the wall of each aneurysm. At the distal end of both aneurysms, however, a characteristic rise in wall pressure is seen when the flow is decelerating or, alternatively, a sharp pressure drop when flow acceleration takes place. The converging–diverging walls of the model seem to have a negligible effect on the pressure distribution, except for those stages of the flow where the acceleration or deceleration is small. *i.e.*, when a change of phase of the flow waveform occurs. The wall pressure distribution is also time dependent. The pulsatile

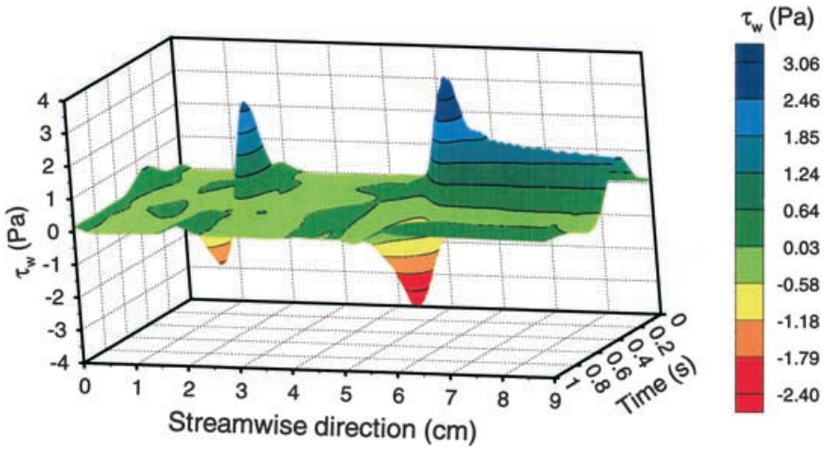

FIGURE 5 Wall shear stress distribution for $Re_m = 300$ as a function of time and axial location.

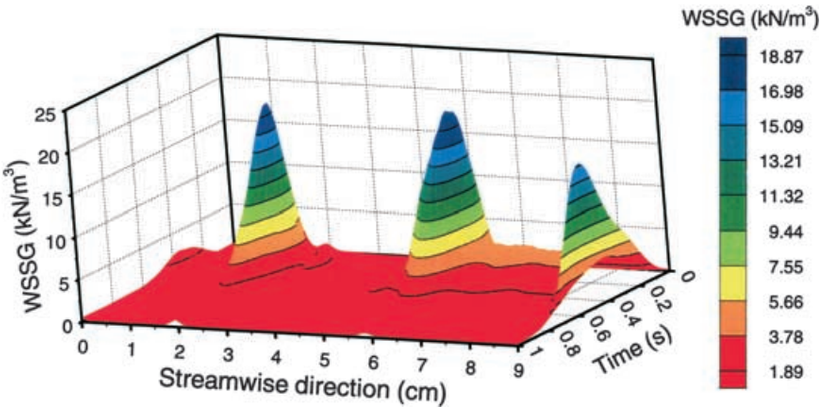

FIGURE 6 Wall Shear Stress Gradient (WSSG) distribution for $Re_m = 300$ as a function of time and axial location.

nature of the flow produces oscillating wall pressure patterns whose distribution tends to follow the multiphasic characteristics of the pulse waveform.

Wall Shear Stress

Figure 5 shows shear stresses along the artery wall for $Re_m = 300$. An oscillatory behavior characterizes the shear stress, having a low magnitude at the center of the aneurysm walls at any stage of the cycle. At the distal end of each aneurysm, there is a drop in the shear stress followed by a sharp high positive peak. These regions of low and high shear stresses are present at all times during the cycle and are time dependent, following a pattern similar to the flow waveform. The spatial variations of the wall shear stress are larger in magnitude at the distal end of the large aneurysm, denoting the effect of aneurysm diameter on this hemodynamic load. Maximum positive shear stress at both distal ends occurs at peak flow, while minimum negative shear stress occurs during systolic deceleration at $t = 0.40$ s.

Wall Shear Stress Gradient

Vortex structures, non-uniform fluid shear stress and high wall pressure are typically associated with *in-vivo* disturbed flow conditions in localized regions of the cardiovascular system commonly subject to diagnosis of arterial diseases. The occurrence of these hemodynamic disturbances has been correlated *in-vitro* with the alignment and migration of endothelial cells, and changes in cell metabolic functions [23,24]. Experimental measurements of non-uniform time–average shear stress at sites where irregular geometries take place in the arterial tree have led to the concept of shear stress gradient as a hemodynamic indicator of potential importance for explaining flow-induced arterial wall pathology and morphological changes in the inner wall lining. Furthermore, the combination of maximum (positive) and minimum (negative) wall shear stresses at the distal end of aneurysm models under steady flow conditions has been shown to promote thrombus formation. Those platelets that have elevated histories of shear stress, while being trapped within a recirculation region, have a higher

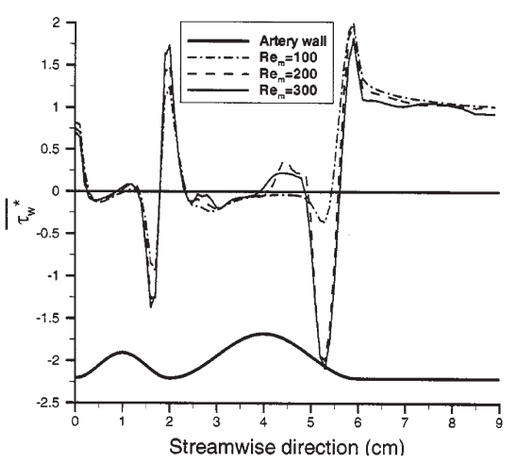

FIGURE 7 Axial distribution of time–average nondimensional wall shear stress ($\overline{\tau_w}^*$) for different time–average Reynolds numbers.

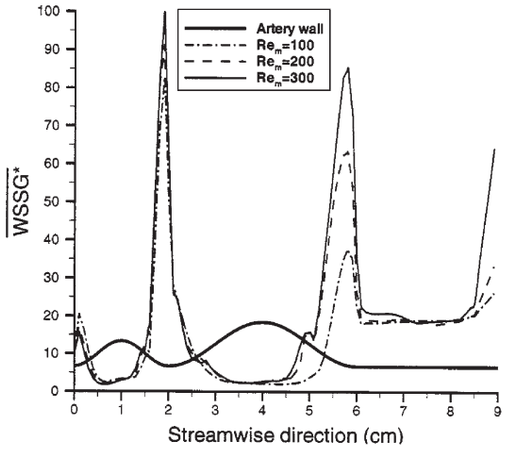

FIGURE 8 Axial distribution of time–average nondimensional wall shear stress gradient ($\overline{\text{WSSG}}^*$) for different time–average Reynolds numbers.

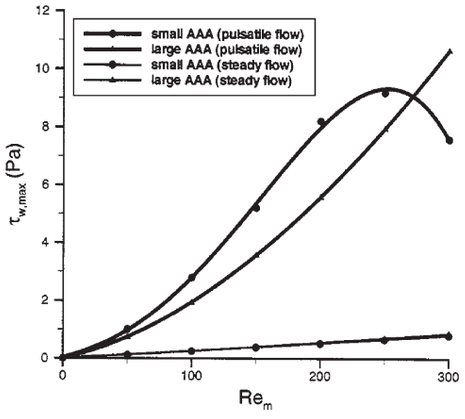

FIGURE 9 Comparison of maximum wall shear stress as a function of time–average Reynolds number for steady and pulsatile flow at C (t = 0.32 s).

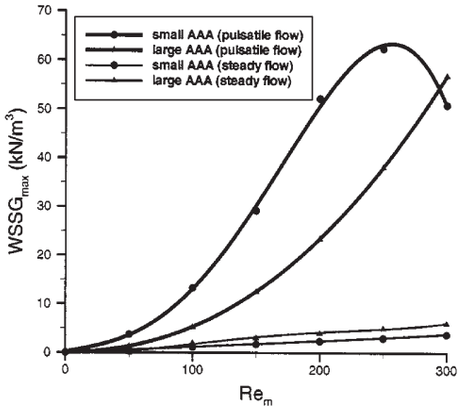

FIGURE 10 Comparison of maximum wall shear stress gradient as a function of time–average Reynolds number for steady and pulsatile flow at C (t = 0.32 s).

incidence of activation and are shown to deposit at the wall in areas of low wall shear stress [7]. Consequently, evaluating gradients of wall shear stress in AAAs would give an indication of those regions where high platelet deposition rates should be expected and where thrombus formation would initiate inside the aneurysm. Therefore, we present the gradient of fluid shear stress evaluated in the tangential and normal directions to the arterial wall as a relevant hemodynamic indicator of pulsatile blood flow in AAAs.

The Wall Shear Stress Gradient (WSSG) distribution for $Re_m = 300$ is shown in Figure 6. Similarly to Figures 4 and 5, this three-dimensional representation of WSSG is a smoothed output of the actual distribution and it is presented in this section only for a qualitative description. The low, almost constant shear stress at the center of the aneurysm walls produces a constant WSSG of near-zero magnitude during the pulsatile cycle at these locations. At the proximal (upstream) and distal (downstream) ends of each aneurysm, however, the oscillatory behavior of the WSSG distribution is characterized by spatial variations at the sites where large velocity gradients occur. The regions where high positive and low negative shear stresses coexist due to flow reattachment are subject to high WSSG values which are maximum at t = 0.31 s, when peak flow is obtained. Moderate levels of WSSG are obtained in both aneurysms during the accelerating (early systole and early diastole) and decelerating (late systole) phases of the cycle. This is explained by the fact that during temporal acceleration (consider $0.20\,s \le t \le 0.30\,s$, for example), vortex shedding and flow separation occurs earlier in the small aneurysm, producing higher shear stresses in the distal end. Alternatively, temporal deceleration induces secondary recirculation regions within the large aneurysm (*e.g.*, $0.32\,s \le t \le 0.50\,s$), which result in an additional change of sign in the shear stress at the wall near the point of flow reattachment. At peak values of flow rate where temporal acceleration is essentially zero (t = 0.31 s and t = 0.52 s), aneurysm size determines the magnitude of the shear stress distribution, resulting in higher WSSGs in the large aneurysm. No information is presently available in the literature on measurements of WSSGs in aneurysms.

The role of wall shear stress gradients in specific arterial diseases is not thoroughly understood yet. Our numerical results for pulsatile flow point to an intermediate stage of aneurysm growth for which disturbed flow conditions exist. The quantification of this disturbance results in three distinct regions of flow development: (i) very low wall shear stresses at the center of a bulge region; (ii) high wall shear stress gradients in the distal end of each bulge; and (iii) oscillating wall shear stresses and wall shear stress gradients throughout each bulge. The oscillatory nature of the WSSG at high time–average volume flow rates, once the aneurysm has begun to grow, produces maximum values of a periodic, pulsating hemodynamic force that may be responsible for severe sites of injury to the inner wall over a relatively long period of time.

Hemodynamic Indicator Functions

The time–average nondimensional wall shear stress ($\overline{\tau_w}^*$) and the time–average nondimensional Wall Shear Stress Gradient ($\overline{WSSG}^*$) are shown in Figures 7 and 8, respectively. These indicators are used to determine average values of shear stress and shear stress gradient at specific points along the wall. Figure 7 shows the spatial variation of the time–average nondimensional wall shear stress for different time-dependent Reynolds numbers. While the value of ($\overline{\tau_w}^*$) in the diverging section of the small aneurysm is about the same for all Re_m, minimum (negative) and maximum (positive) wall shear stresses in the converging region increase in magnitude with the Reynolds number, resulting in a distribution where there are three sign changes of the indicator along the wall. Similarly for the large aneurysm, the presence of clockwise-rotating vortices for $Re_m = 200$ and $Re_m = 300$ results in a positive time–average wall shear stress region in the converging section of the aneurysm, close to

TABLE I Correlation coefficients for maximum wall shear stress and wall shear stress gradient as a function of the time–average Reynolds number at C (t = 0.32 s), according to Eq. (4)

Hemodynamic indicator		Correlation coefficients				
		$a_4 \times 10^{10}$	$a_3 \times 10^{7}$	$a_2 \times 10^{4}$	$a_1 \times 10^{2}$	$a_0 \times 10^{2}$
$\tau_{w,max}$	small AAA	−38.76	9.833	0.955	1.222	1.542
	large AAA	0.460	−0.732	1.037	0.972	0.114
$WSSG_{max}$	small AAA	−421.4	149.2	−2.970	5.254	7.176
	large AAA	−8.511	9.297	4.221	0.203	0.015

its center. Unlike steady-flow wall shear stress distributions [19], these regions are characterized by predominantly positive instantaneous shear stresses throughout the pulsatile cycle, and are given by 1.0 cm ≤ z ≤ 1.35 cm for the small aneurysm and 4.0 cm ≤ z ≤ 4.92 cm for the large aneurysm.

The spatial variation of the time–average non-dimensional wall shear stress gradient is shown in Figure 8. The $\overline{WSSG}^*$ at the entrance is due to the change in wall shear stress from the Poiseuille-flow value to the negative wall shear stress obtained at the point of flow separation in the small aneurysm. The variation of shear stress at this point is more significant in the direction normal to the wall than in the tangential direction. The negative wall shear stress obtained after flow separation in the small aneurysm has an almost constant value until reaching the distal end, and thus a near-zero $\overline{WSSG}^*$ is obtained for $100 \leq Re_m \leq 300$ for 0.41 cm < z < 1.25 cm. High levels of $\overline{WSSG}^*$ are obtained at the site of flow reattachment. The change of sign of the wall shear stress at this location and its increase further downstream results in a peak of the $\overline{WSSG}^*$ curves. The pattern for $\overline{WSSG}^*$ distribution is similar for the large aneurysm. Flow separation occurs proximally producing a non-zero $\overline{WSSG}^*$ at the entrance of the large aneurysm; this value is greater than the inlet $\overline{WSSG}^*$ because the negative velocity gradient in the proximal end of the large aneurysm is larger than in the small aneurysm.

Correlation Functions

The discussions based on Figures 4–8 point out that the distal end of an aneurysm is subject to the highest wall shear stresses and WSSGs in the vicinity of a point of flow reattachment. Therefore, we have developed correlations for the region where aneurysm rupture is most likely to occur [25]. A fourth order polynomial function of the form shown in Eq. (4) is used to correlate the wall hemodynamics with the time–average Reynolds number, where $\xi = f(Re_m, t)$ is the hemodynamic indicator evaluated at the wall (τ_w or WSSG) at a given time during the pulsatile flow cycle.

$$\xi_w(t) = \sum_{i=0}^{4} a_i Re_m^i \tag{4}$$

Table I shows the coefficients (in the appropriate units) resulting from the correlations at t = 0.32 s (near peak flow). These correlations are used to compare the variation of maximum wall shear stress and WSSG with Re_m, for pulsatile flow at t = 0.32 s and for steady flow, as shown in Figures 9 and 10.

A monotonic increase of the maximum (positive) wall shear stress is shown in Figure 9 for the large aneurysm. The maximum shear stress in the large aneurysm is greater than the one in the small aneurysm only for $Re_m \geq 270$. The temporal development of vortex structures discussed earlier accounts for this behavior. For $Re_m < 270$, the recirculation region begins to fill in the small aneurysm before flow separation takes place in the large aneurysm, indicating that at t = 0.32 s the velocity gradients in the small aneurysm are stronger than in the large aneurysm. For higher Reynolds numbers ($Re_m \geq 270$), where flow separation occurs before peak flow (*e.g.*, $t_{separation} = 0.29$ s for $Re_m = 300$), reversed flow already fills the proximal half of the large aneurysm at t = 0.30 s. This yields a higher maximum shear stress in the large aneurysm. A similar pattern is shown for $WSSG_{max}$ in Figure 10, where for $Re_m \geq 290$ the maximum WSSG in the large aneurysm is greater than the one in the small aneurysm. The intersection of the curves for $WSSG_{max}$ and $\tau_{w,max}$ does not occur at the same Re_m; this is explained by evaluating the contribution of the individual terms of the WSSG function, as given by Eq. (4) in Part I of this investigation [19]. The WSSG in the tangential direction ($\partial \tau_w / \partial \hat{t}$) is greater in the large aneurysm than in the small aneurysm, for the range $270 \leq Re_m \leq 290$. The shear stress gradient in the direction normal to the wall ($\partial \tau_w / \partial \hat{n}$), however, is much smaller in the distal end of the large aneurysm, where $WSSG_{max}$ occurs. Because the vortex is at an early stage of development, closer to the diverging wall of the large aneurysm, the distribution of the streamlines at this location for t = 0.32 s indicates a region of forward flow. Therefore, the contribution of the $\partial \tau_w / \partial \hat{n}$ term is significant in the pattern of the $WSSG_{max}$ distribution for the range $270 \leq Re_m \leq 290$. A comparison between steady and pulsatile flow wall stresses indicates that the maximum wall shear stress in the small aneurysm for pulsatile flow at t = 0.32 s is up to 15.8 times the wall shear stress for steady flow, which occurs for $Re_m = 200$. Additionally, the $WSSG_{max}$ for pulsatile flow in the small aneurysm is 9.5 times greater than its steady flow counterpart for $Re_m = 300$.

CONCLUSIONS AND CURRENT WORK

The vortex structure induced by pulsatile blood flow in aneurysms is characterized by means of a sequence of different flow stages in one period of the pulsatile flow cycle. Five distinct flow phases depict the vortex dynamics, which are Reynolds number-dependent and aneurysm-size-dependent:

i) *Early systolic acceleration* involves shedding of the vortices left from the previous cycle, resulting in attached flow patterns. Vortices in the small aneurysm are swept earlier than in the large aneurysm.
ii) *Late systolic acceleration* is characterized by attached flow for low time–average Reynolds numbers ($Re_m \leq 100$). For high Re_m, the decrease in the temporal acceleration of the fluid upon reaching peak flow causes flow separation in the proximal ends of both aneurysms. The ring-shaped vortex forms earlier in the small aneurysm.
iii) *Systolic deceleration* involves vortex growth and translation of vortex centers downstream. For high Re_m, secondary clockwise-rotating vortices are induced near the center of both aneurysms after the main recirculation regions grow to full size.
iv) *Early diastole* is characterized by partial shedding of the vortex structures left from systole, driven by a favorable pressure gradient. As the flow attempts to reattach to the wall, the recirculation regions are reduced considerably in size.
v) *Late diastole* involves vortices of fairly constant size inside both aneurysms. For high time–average Reynolds numbers, secondary vortices coexist with the main recirculation region at the center of the large aneurysm.

The temporal evolution of the flow patterns influences the spatial distribution and oscillatory behavior of hemodynamic indicators such as the instantaneous wall pressure, wall shear stress and WSSG. At peak flow, the highest wall shear stress and WSSG levels are obtained at the distal end of both aneurysms. Time-dependent flow results demonstrate that the converging region of an aneurysm is cyclically exposed to high and low hemodynamic wall stresses. These stresses oscillate in time and are higher for a large aneurysm (*i.e.*, greater maximum diameter and length) than for a small aneurysm, at the same time–average Reynolds number.

It is unlikely that an aneurysm of medium or large size ($D > 4.5\,cm$) would be axisymmetric. AAAs in an advanced stage of growth are truly asymmetric, due to the presence of tissue surrounding the abdominal aorta and to the vertebral column located posterior to this artery segment. This makes a large AAA less fusiform and to grow apart from the lumen's centreline, accounting for a major anterior dilation and a more flat posterior surface. Therefore, the conclusions drawn on the basis of these axisymmetric hemodynamic stress calculations may only hold qualitatively for real three-dimensional asymmetric models. Further investigation based on asymmetric aneurysm models is currently been conducted using a novel formulation for the calculation of three-dimensional wall shear stresses. This formulation is based on a projection of the shear stress tensor in the tangential direction of the wall [26–28]. Imaginary planes that intersect the wall surface enclosing the longitudinal axis are used to balance forces at the wall and a two-dimensional resultant force is obtained as a function of all six independent stress components.

Acknowledgements

The authors gratefully acknowledge the support of the National Science Foundation grant CTS-9630801, the Whitaker Foundation grant RG-96-0202, and the Pennsylvania Infrastructure Technology Alliance Partnership from the Commonwealth of Pennsylvania's Department of Economic and Community Development.

References

[1] Wille, S. (1981) "Pulsatile Pressure and Flow in an Arterial Aneurysm Simulated in a Mathematical Model", *Journal of Biomedical Engineering* **3**, 153–158.
[2] Perktold, K. (1987) "On the Paths of Fluid Particles in an Axisymmetrical Aneurysm", *Journal of Biomechanics* **20**, 311–417.
[3] Fukushima, T., Matsusawa, T. and Homma, T. (1989) "Visualization and Finite Element Analysis of Pulsatile Flow in Models of the Abdominal Aortic Aneurysm", *Biorheology* **26**, 109–130.
[4] Taylor, T. and Yamaguchi, T. (1994) "Three-Dimensional Simulation of Blood Flow in an Abdominal Aortic Aneurysm–Steady and Unsteady Flow Cases", *ASME Journal of Biomechanical Engineering* **116**, 89–97.
[5] Elger, D., Slippy, J., Budwig, R., Khraishi, T. and Johansen, K. (1995) "A Numerical Study of the Hemodynamics in a Model Abdominal Aortic Aneurysm (AAA)", In: Gerbsch, R.A. and Ohba, K., eds, Proceedings of the ASME Symposium on Biomedical Fluids Engineering **FED-212**, pp 15–22.
[6] Khraishi, T., Elger, D., Budwig, R. and Johansen, K. (1996) "The Effects of Modeling Parameters on the Hemodynamics of an Abdominal Aortic Aneurysm (AAA)", Proceedings of the 1996 ASME Fluids Engineering Division Summer Meeting **FED-237**, pp 349–356.
[7] Bluestein, D., Niu, L., Schoephoerster, R. and Dewanjee, M. (1996) "Steady Flow in an Aneurysm Model: Correlation between Fluid Dynamics and Blood Platelet Deposition", *ASME Journal of Biomechanical Engineering* **118**, 280–286.
[8] Guzmán, A. and Amon, C. (1996) "Dynamical Flow Characterization of Transitional and Chaotic Regimes in Converging–Diverging Channels", *Journal of Fluid Mechanics* **321**, 25–57.
[9] Amon, C., Guzmán, A. and Morel, B. (1996) "Lagrangian Chaos, Eulerian Chaos, and Mixing Enhancement in Converging–Diverging Channel Flows", *Physics of Fluids* **8**, 1192–1206.
[10] Viswanath, N., Zajac, S. and Rodkiewicz, C. (1997) "On the Abdominal Aortic Aneurysms: Pulsatile State Considerations", *Medical Engineering and Physics* **19**, 343–351.
[11] Moraga, N., Guzmán, A. and Rosas, C. (1997) "Mecánica de Fluidos No Newtonianos de Flujo Transiente en Tubería con Sección Transversal Variable en el Espacio", VI Congreso La Ingeniería en la Industria del Cobre (Universidad de Antofagasta, Chile), pp 167–175.
[12] Guzmán, A., Moraga, N. and Amon, C. (1997) "Pulsatile Non-Newtonian Flow in a Double Aneurysm", Proceedings of the 1997 ASME International Mechanical Engineering Congress and Exposition, pp 87–88.

[13] Egelhoff, C., Budwig, R., Elger, D., Khraishi, T. and Johansen, K. (1999) "Model Studies of the Flow in Abdominal Aortic Aneurysms during Resting and Exercise Conditions", *Journal of Biomechanics* **32**, 1319–1329.

[14] Peattie, R. and Bluth, E. (1998) "Experimental Study of Pulsatile Flows in Models of Abdominal Aortic Aneurysms", *Proceedings of the 20th Annual International Conference of the IEEE Engineering in Medicine and Biology Society* **20**, 367–370.

[15] Yu, S. (2000) "Steady and Pulsatile Flow Studies in Abdominal Aortic Aneurysm Models using Particle Image Velocimetry", *International Journal of Heat and Fluid Flow* **21**, 74–83.

[16] DePaola, N., Gimbrone, M., Davies, P. and Dewey, C. (1992) "Vascular Endothelium Responds to Fluid Shear Stress Gradients", *Arteriosclerosis and Thrombosis* **12**, 1254–1257.

[17] Davies, P., Mundel, T. and Barbee, K. (1995) "A Mechanism for Heterogeneous Endothelial Responses to Flow *In Vivo* and *In Vitro*", *Journal of Biomechanics* **28**, 1553–1560.

[18] Grabowski, E. (1995) "Thrombolysis, Flow, and Vessel Wall Interactions", *Journal of Vascular and Interventional Radiology* **6**, 25S–29S.

[19] Finol, E. and Amon, C. (2001) "Flow-Induced Stresses in Abdominal Aortic Aneurysms: Part I-Steady Flow Hemodynamics", *Computer Methods in Biomechanics and Biomedical Engineering* **5**(4), 309–318.

[20] Milnor, W. (1989) Hemodynamics, 2nd Ed. (Wilkins and Wilkins, Baltimore, MD).

[21] Mills, C., Gabe, I., Gault, J., Mason, D., Ross, Jr, J., Braunwald, E. and Shillingford, J. (1970) "Pressure-flow Relationships and Vascular Impedance in Man", *Cardiovascular Research* **4**, 405–417.

[22] Pedersen, E., Sung, H., Burlson, A. and Yoganathan, A. (1993) "Two-Dimensional Velocity Measurements in a Pulsatile Flow Model of the Normal Abdominal Aorta simulating different Hemodynamic Conditions", *Journal of Biomechanics* **26**, 1237–1247.

[23] Davies, P. (1997) "Mechanisms Involved in Endothelial Responses to Hemodynamic Forces", *Atherosclerosis* **131**, S15–S17.

[24] Shen, J., Luscinkas, F., Connolly, A., Dewey, C. and Gimbrone, M. (1992) "Fluid Shear Stress Modulates Cytosolic Free Calcium in Vascular Endothelial Cells", *American Journal of Physiology* **262**, C384–C390.

[25] Muraki, N. (1983) "Ultrasonic Studies of the Abdominal Aorta with Special Reference to Hemodynamic Considerations on Thrombus Formation in the Abdominal Aortic Aneurysm", *Journal of Japanese College Angiology* **23**, 401–413.

[26] Finol, E. and Amon, C. (2000) "On the Calculation of Fluid Shear Stresses at the Wall of Dilated Large Arteries: Part I–Application to 2D Axisymmetric Computational Models", Advances in Bioengineering: Proceedings of the 2000 ASME International Mechanical Engineering Congress and Exposition–IMECE 2000 **48**, pp 97–98.

[27] Finol, E. and Amon, C. (2000) "On the Calculation of Fluid Shear Stresses at the Wall of Dilated Large Arteries: Part II–Application to 3D Computational Models", Advances in Bioengineering: Proceedings of the 2000 ASME International Mechanical Engineering Congress and Exposition–IMECE 2000 **48**, pp 13–14.

[28] Finol, E. and Amon, C. (2001) "Blood Flow in Abdominal Aortic Aneurysms: Pulsatile Flow Hemodynamics", *ASME Journal of Biomechanical Engineering*, in press.